

High Brightness HDR Projection Using Dynamic Freeform Lensing

GERWIN DAMBERG and JAMES GREGSON

University of British Columbia
and

WOLFGANG HEIDRICH

King Abdullah University of Science and Technology and University of British Columbia

Cinema projectors need to compete with home theater displays in terms of image quality. High frame rate and spatial resolution as well as stereoscopic 3D are common features today, but even the most advanced cinema projectors lack in-scene contrast and, more important, high peak luminance, both of which are essential perceptual attributes of images appearing realistic. At the same time, HDR image statistics suggest that the average image intensity in a controlled ambient viewing environment such as the cinema can be as low as 1% for cinematic HDR content and not often higher than 18%, *middle gray* in photography. Traditional projection systems form images and colors by blocking the source light from a lamp, therefore attenuating between 99% and 82% of light, on average. This inefficient use of light poses significant challenges for achieving higher peak brightness levels.

In this work, we propose a new projector architecture built around commercially available components, in which light can be steered to form images. The gain in system efficiency significantly reduces the total cost of ownership of a projector (fewer components and lower operating cost), and at the same time increases peak luminance and improves black level beyond what is practically achievable with incumbent projector technologies. At the heart of this computational display technology is a new projector hardware design using phase modulation in combination with a new optimization algorithm that is capable of on-the-fly computation of freeform lens surfaces.

Categories and Subject Descriptors: I.3.3 [Computer Graphics]: Three-Dimensional Graphics and Realism—*Display Algorithms*

General Terms: Freeform lensing, high dynamic range projection, caustics

Additional Key Words and Phrases: Laser projector, high brightness, visual perception, image statistics, high peak luminance

Authors' addresses: G. Damberg, J. Gregson, and W. Heidrich, Department of Computer Science, The University of British Columbia, 2366 Main Mall, Vancouver, BC V6T 1Z4, Canada; emails: gdamberg@cs.ubc.ca, jgregson@cs.ubc.ca, heidrich@cs.ubc.ca.

Permission to make digital or hard copies of part or all of this work for personal or classroom use is granted without fee provided that copies are not made or distributed for profit or commercial advantage and that copies show this notice on the first page or initial screen of a display along with the full citation. Copyrights for components of this work owned by others than ACM must be honored. Abstracting with credit is permitted. To copy otherwise, to republish, to post on servers, to redistribute to lists, or to use any component of this work in other works requires prior specific permission and/or a fee. Permissions may be requested from Publications Dept., ACM, Inc., 2 Penn Plaza, Suite 701, New York, NY 10121-0701 USA, fax +1 (212) 869-0481, or permissions@acm.org.

© 2016 ACM 0730-0301/2016/04-ART24 \$15.00

DOI: <http://dx.doi.org/10.1145/2857051>

ACM Reference Format:

Gerwin Damberg, James Gregson, and Wolfgang Heidrich. 2016. High brightness HDR projection using dynamic freeform lensing. *ACM Trans. Graph.* 35, 3, Article 24 (April 2016), 11 pages.
DOI: <http://dx.doi.org/10.1145/2857051>

1. INTRODUCTION

Ideally, high dynamic range (HDR) projectors *should* produce both darker black and (much) brighter highlights, while at the same time maintaining an appropriate-for-the-viewing-environment average picture level (APL). However, today's HDR projectors predominantly focus on improving black level (e.g., recently demonstrated laser projection systems by Kodak, IMAX, Zeiss, Dolby, Barco, Christie, and others). Improved contrast *and* peak luminance are vital for higher perceived image quality (brightness, colorfulness) [Rempel et al. 2009]. Brightness perception of luminance levels is near-logarithmic in the photopic range. Doubling the luminance of an image feature on a projection screen (e.g., by increasing the lamp power of a traditional projector by $2\times$) does not result in a significant improvement in perceived brightness.

Results in Rempel et al. [2011], Reinhard et al. [2012], and Zink and Smith [2015] suggest that $10\times$, $20\times$, or even $100\times$ increases in peak luminance would be desirable, even if most images require only a very small percentage of pixels to be this bright (see Section 3.1).

Such drastic improvements cannot be achieved with conventional projector designs, which use amplitude spatial light modulators (SLMs) to generate images by pixel-selectively blocking light. For a typical scene, this process destroys between 82% and 99% of the light that *could* reach the screen, with the energy being dissipated as heat. This causes a number of engineering challenges, including excessive power consumption, thermal engineering, and cost, which ultimately limit the peak luminance in current projector designs.

In this article, we explore the use of *dynamic* freeform lenses in the context of light-efficient, high (local) peak luminance, and high-contrast (HDR) projection systems. Freeform lenses, that is, aspherical, asymmetric lenses have recently received a lot of attention in optics as well as computer graphics. In the latter community, freeform lenses have mostly been considered under the auspices of *goal-based caustics*, that is, the design of lenses that generate a specific caustic image under predefined illumination conditions [Finckh et al. 2010; Papas et al. 2011; Schwartzburg et al. 2014; Yue et al. 2014].

We implement dynamic freeform lensing on a *phase-only* SLM, which is combined with a conventional light blocking device such as a reflective LCD in a new type of cascaded modulation approach. The phase modulator in our approach creates a smooth, but still quite detailed, *caustic* image on the amplitude modulator. Since the caustic image merely redistributes, or *reallocates*, light [Hoskinson et al. 2010], this approach produces both a higher dynamic range as well as an improved (local) peak luminance as compared to conventional projectors.

This work is based on our earlier work on generating freeform lenses or goal-driven caustics using common approximations in optics to directly optimize the phase modulation pattern or lens shape of a freeform lens Damberg and Heidrich [2015]. The method is briefly reviewed in Section 3.2. In the current work, we make the following new contributions:

- a new Fourier domain optimization approach for generating freeform lenses that is capable of high frame rates for dynamic light steering using phase modulators;
- a new dual-modulation projector design that combines one phase and one amplitude modulator for image generation and enables high-brightness, high-contrast images.

To our knowledge, this is both the first time that practical, high-resolution light redistribution has been shown using *commercially available* hardware and the first time that phase-only SLMs have been used for dynamic freeform lensing.

2. RELATED WORK

Our research draws from a number of different fields of related work, including both display technologies and algorithms for freeform lens design. The following is a brief description of the state of the art in several related fields.

2.1 Dynamic Contrast, Irises and Global Light Source Dimming

The performance of projector systems and other types of displays is often advertised in terms of *dynamic contrast*, which relates to the sequential measurement of the intensity of a “full white” image and a “full black” image. Dynamic contrast ratings can be increased significantly with projector architectures that can globally modulate the intensity of the image, for example, by dimming the light source (for solid-state lighting such as LED or laser projectors), or through the use of a mechanical iris (for high-pressure discharge lamps that cannot be dimmed). In product marketing material, the quoted sequential contrast numbers for these types of projectors often exceed 1,000,000:1. Although projectors with high dynamic contrast provide an improved viewing experience by allowing “mood adaptations” according to image content, these numbers are not indicative of true HDR performance, since simultaneous in-scene contrast is typically only between 1,000:1 and 6,000:1. In our work, we aim for true HDR projection with simultaneously brighter peak luminance and deeper black levels, while limiting power consumption.

2.2 Dual Modulation Projection Displays

Over the last two decades, there have been several different proposals to implement dual modulation approaches in display applications to increase in-scene contrast. The availability of large flat-panel TVs and high-power LEDs led to an adoption of dual modulation techniques in consumer electronics [Seetzen et al. 2004]. Similar concepts to increase contrast in projectors include screens with spatially varying reflectivity (either statically [Bimber and Iwai

2008] or dynamically [Seetzen 2009]), and arrays of hundreds or even thousands of primitive projectors [Seetzen 2009], proposed as means to increase on-screen luminance. Few of these concepts have made it past the research stage and small-scale prototypes. One exception is dual modulation projector designs using two traditional amplitude SLMs in sequence [Blackham and Neale 1998; Damberg et al. 2007a, 2007b; Kusakabe et al. 2009]. These systems are typically intended for specialty applications requiring very good black level and limited peak luminance. The low optical efficiency of amplitude SLMs results in both a low light intensity on screen and high power consumption, all at significantly increased system cost. Nevertheless, dual amplitude attenuating projectors are being deployed not only in planetariums, training, and simulation applications, but recently also in high-end, *premium large-format* cinema.

To alleviate the problem of inefficient image formation, Hoskinson et al. [2010, 2012] introduced the notion of *light reallocation* using 2D arrays of tip-tilt mirrors in the light path of a small DLP projector, whereby the first modulator does not actually absorb much light, but moves it around within the image plane so that it can be reallocated from dark-image regions to bright ones, essentially creating moving bright spots of approximately constant size on the amplitude modulator. Hoskinson et al. [2010, 2012] used a continuously tilting micro-mirror array to achieve this light reallocation. Unfortunately, such mirror arrays are not easy to control accurately (achieving predictable tilt angles for a given drive signal) and are still only available as research prototypes at low spatial resolution (7×4 pixels in their work).

In our work, we achieve high-contrast light steering by employing a readily available 2 megapixel LCoS SLM operated in a phase-only fashion. Instead of computationally determining independent mirror tilt angles, we optimize a continuous phase function representing the required curvature of the wavefront of light as it passes through the SLM.

2.3 Holographic Displays

Holographic image formation models (e.g., Lesem et al. [1969]) have been adapted to create digital holograms [Haugen et al. 1983] quite early in the history of phase SLMs. Holographic projection systems have been proposed in many variations for research and specialty applications, including pocket projectors [Buckley 2008]. Some projection systems use diffraction patterns addressed on a Ferroelectric Liquid Crystal Display (FLCD) in combination with temporally and spatially coherent light for image generation. The challenges in holography for projectors lie in achieving sufficiently good image quality. Since holograms are optimized in the Fourier domain, the resulting phase masks exhibit very high spatial frequencies, which severely limits the diffraction efficiency, especially when combined with low-resolution and/or binary phase modulators. By comparison, we note that our method is not based on Fourier optics (in fact, it follows a geometric optics image formation model), and generates phase masks that are piecewise smooth spatially, similar to a Fresnel lens.

2.4 Freeform Lenses

Recently, there has been increased interest in freeform lens design, both for general lighting applications (e.g., Miñano et al. [2009]) and for goal-based caustics [Berry 2006; Hullin et al. 2013]. In the latter application, we can distinguish between discrete optimization methods that work on a pixelated version of the problem (e.g., Papas et al. [2011, 2012] and Yue et al. [2012]), and those that optimize for continuous surfaces without obvious pixel structures (e.g., Finckh et al. [2010], Kiser et al. [2013], Pauly and Kiser [2012], Schwartzburg



Fig. 1. Examples from the image set that were used in this study.

et al. [2014], and Yue et al. [2014]). The current state-of-the-art methods define an optimization problem on the gradients of the lens surface, which then have to be integrated into a height field. This leads to a tension between satisfying a data term (the target caustic image) and maintaining the integrability of the gradient field.

In our previous work Damberg and Heidrich [2015], a simplified new formulation is derived in which we optimize directly for the phase function (i.e., the shape of the wavefront in the lens plane) or, equivalently, the lens shape, without a need for a subsequent integration step. This is made possible by a new parameterization of the problem that allows expression of the optimization directly in the lens plane rather than the image plane. The formulation, which is summarized in Section 3.2, also serves as the basis for the development of our new real-time algorithm (Section 4).

2.5 Lens and Phase Function Equivalence

The effects of phase delays introduced by a smooth phase function can be related to an equivalent physical refractive lens under the paraxial approximation, which can be derived using either geometric optics or from the Huygens principle. The paraxial approximation is widely used in optics and holds when $\sin \theta \approx \theta$. For the projection system considered in this article, $|\theta| \leq 12^\circ$, which corresponds to redirecting light from one side of the image to the other. The error in the paraxial approximation is less than 1% for this case, which makes optimizing directly for the phase surface possible.

3. BACKGROUND

3.1 HDR Luminance Requirements in Cinema

Little high-brightness HDR video content is publicly available that has been color graded for a theatrical viewing environment. Partially, this is due to the current lack of sufficiently capable large-screen projection systems. In this section, we attempt to estimate the relative power required to reproduce HDR luminance levels up to 10X above current peak luminance in cinema using color-graded HDR still images. An analysis of 104 HDR images has been performed, and power requirements for a light steering projector as in the proposed architecture have been estimated. In this theoretical exercise, it was found that a light-steering projector with less power than a traditional cinema projector can directly reproduce all images up to 48cd/m^2 and almost all of the surveyed HDR images up to 480cd/m^2 without the need for additional tonal compression. Table I summarizes the results.

3.1.1 Methodology. Fairchild's [2007] set of 104 scene-referred HDR images was analyzed (see Figure 1 for examples). The images differ in dynamic range from less than 1,000 : 1 to over 10^9 : 1. Most images are outdoor scenes. While the image data represents measured, scene-referred HDR (actual scene luminance levels) and is not intended for viewing on a cinema projector, an initial guess for a cinema-suitable rendering can be established by shifting the image intensity so that the APL approximately matches the estimated viewer adaptation level in the cinema. A simple linear scaling operator, $S_{adaptation}$, was determined manually for each image. Images were hand-tuned in a dark viewing environment,

Table I. Power Required to Reproduce the Images from the HDR Data Set on Three Different Projectors (Relative to a Standard Cinema Projector in the First Row)

L_{peak}	Steering?	P_{rel} (min)	P_{rel} (median)	P_{rel} 90%tile
48cd/m^2	no	1	1	1
48cd/m^2	yes	0.0107	0.1079	0.2595
480cd/m^2	yes	0.0107	0.1832	0.8554

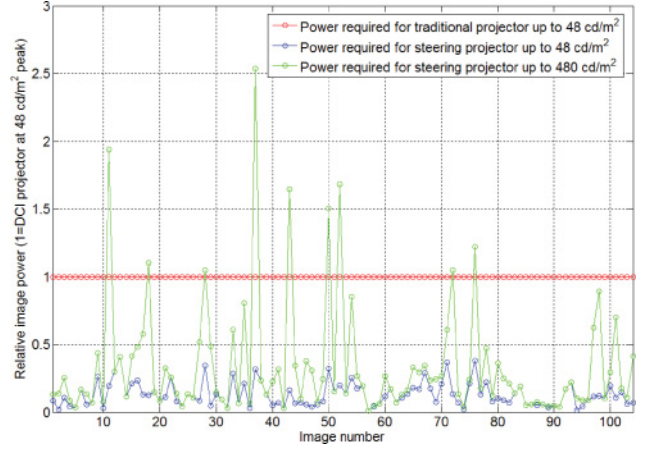


Fig. 2. Relative power required to reproduce each of 104 HDR images on three hypothetical projectors: two light-steering projectors with a peak luminance of 48cd/m^2 (blue) and 480cd/m^2 (green) relative to a traditional, light blocking cinema projector with peak luminance of 48cd/m^2 (red). The average power required to achieve identical peak luminance (48cd/m^2) is on the order of 13% of a traditional projector. More important, all but the very brightest images (approximately 9% of all images under test), can be reproduced up to a peak luminance of 480cd/m^2 while using less or the same amount of power.

on a calibrated 27" reference monitor (Dell U2713HMT, calibration confirmed using a Photo Research Inc. PR-650 spectro-radiometer), which was set to a peak white luminance of 48cd/m^2 (D65 white point). While adjusting the intensity, the images were viewed from a distance of approximately 3-5 screen-heights.

Once an adequate brightness scaling factor had been determined, luminance levels above 10X that of full-screen white (FSW), 480cd/m^2 , were clipped. Next, the steering efficiency of the proposed projector architecture was accounted for via a system PSF approximation (in this case, a somewhat conservative, large Gaussian kernel spanning effectively 81 pixels of 1920 horizontal image pixels). The mean intensity across all pixels of the resulting luminance profile serves as an approximate metric for power requirements of a light-steering projector.

3.1.2 Computational Steps.

- Compute scaled luminance: $Y_s = Y_{hdr} \times S_{adaptation}$
- Clip Y_s to $10 \times 48\text{cd/m}^2 = 480\text{cd/m}^2$: $Y_{sc} = \min(480, Y_s)$
- Account for steering efficiency: $Y_{scm} = Y_{sc} * g$
- Determine arithmetic mean luminance: $\bar{Y}_{scm} = \text{mean}(Y_{scm})$
- Scale to reference (48cd/m^2): $P_{rel} = \frac{\bar{Y}_{scm}}{48\text{cd/m}^2}$

3.1.3 Results. Figure 2 shows the estimated power required to reproduce each HDR image on a light-steering projector with peak luminance identical to that of a traditional cinema projector, 48cd/m^2 , and of a light-steering projector with a peak luminance one order of magnitude greater than cinema reference systems:

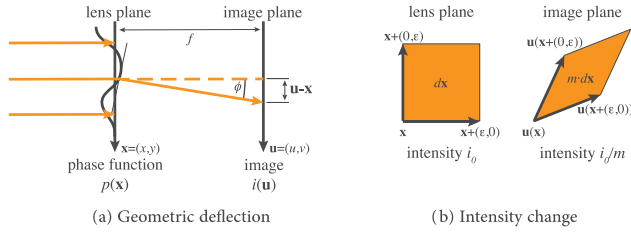


Fig. 3. Left: Geometry for the image formation model, with phase modulation $p(\mathbf{x})$ taking place in the lens plane, and resulting deflections creating a caustic image on the image plane at distance f . Right: The local intensity on the image plane is related to the change in the differential surface area between corresponding patches on the lens plane and the image plane.

480cd/m². All images can be reproduced on the 48cd/m² light-steering architecture using only a fraction of the power (13%) of a traditional projector. More important, almost all images can be reproduced up to 480cd/m² (10X higher peak luminance) using the same or less power compared to a traditional projector.

We note that the APL of our dataset when using the scale and clip operations described earlier with no further artistic color corrections appears higher than what might be expected from cinema-ready high-brightness HDR content. We point the interested reader to Zink and Smith [2015] for a recent introduction to HDR content production, in which significantly lower APLs (3% and less) have been reported. This, in turn, would suggest that the power requirements for a light-steering projector architecture could be even lower (or peak luminance and contrast higher) than proposed in our work. For our comparisons on the HDR prototype projector in Section 5, we select test images within a range of relatively conservative (=high) APLs from 7% to 45% (see Table III, second column).

3.2 Freeform Lensing

In this section, we briefly summarize the basic freeform lensing algorithm [Damberg and Heidrich 2015]. The new algorithmic contributions will then be presented in Section 4.

The basic geometry for freeform lensing using a phase modulator is depicted in Figure 3. A lens plane and an image plane (e.g., a screen) are placed parallel to each other at focal distance f . Collimated light is incident at the lens plane from the normal direction, but a phase modulator (or lens) in the lens plane distorts the phase of the light, resulting in a curved phase function $p(\mathbf{x})$, corresponding to a local deflection of the light rays.

Using the *paraxial approximation* $\sin \phi \approx \phi$, which is valid for small deflection angles, it is possible to show that the geometric displacement in the image plane is proportional to the gradient of the phase function:

$$\mathbf{u}(\mathbf{x}) = \mathbf{x} + f \cdot \nabla p(\mathbf{x}). \quad (1)$$

Likewise, the local intensity of a differential patch on the image plane is determined by the magnification (change in area) between this patch and the corresponding patch on the lens plane (Figure 3, right). This magnification factor $m(\cdot)$ is related to the Laplacian of the phase modulation:

$$m(\mathbf{x}) \approx 1 + f \cdot \nabla^2 p(\mathbf{x}). \quad (2)$$

This yields the following expression for the intensity distribution on the image plane:

$$i(\mathbf{x} + f \cdot \nabla p(\mathbf{x})) = \frac{1}{1 + f \cdot \nabla^2 p(\mathbf{x})}. \quad (3)$$

In other words, the intensity $i(\mathbf{u})$ on the image plane can be directly computed from the Laplacian of the scalar phase function on the lens plane.

This image formation model gives rise to the following optimization problem for determining the phase function $p(\mathbf{x})$ for a given target image $i(\mathbf{u})$:

$$\begin{aligned} \hat{p}(\mathbf{x}) &= \arg \min_{p(\mathbf{x})} \int_{\mathbf{x}} (i_p(\mathbf{x}) - 1 + f \cdot \nabla^2 p(\mathbf{x}))^2 d\mathbf{x} \\ &= \arg \min_{p(\mathbf{x})} F(p(\mathbf{x})), \end{aligned} \quad (4)$$

where i_p is a *warped image* $i_p(\mathbf{x}) = i(\mathbf{x} + f \cdot \nabla p(\mathbf{x}))$ in which the target intensity $i(\mathbf{u})$ in the image plane has been warped backwards onto the lens plane using the distortion $\mathbf{u}(\mathbf{x})$ produced by a given phase function $p(\mathbf{x})$. This optimization problem can be solved by iterating between updates to the phase function and updates to the warped image. Convergence of the algorithm is moderate; thus, the method is not directly suitable for real-time freeform lensing in projection systems.

The computational cost of the algorithm is primarily related to the solution of large-scale biharmonic problems. A Krylov subspace method (QMR) is employed, making it difficult to find an effective preconditioner. The large scale of the system can also be problematic. Efficient solutions to biharmonic systems is an ongoing topic of research, including, for example, preconditioning approaches [Silvester and Mihajlović 2004], multigrid methods [Zhao 2004] and operator splitting schemes [Tang and Christov 2006]. Scaling these approaches to the millions of degrees of freedom that are required for imaging applications in real time is challenging.

In the following section, we introduce a new approach based upon *proximal operators* that allow the problem to be expressed in the Fourier domain and consequently solved efficiently using highly parallelizable fast Fourier transform libraries.

4. REAL-TIME FREEFORM LENSING

The key insight is that, by mirror padding the input image, the system arising from the discretization of ∇^4 results in periodic boundary conditions with pure-Neumann boundary conditions at the nominal image edge. This is illustrated in Figure 4 and was also observed in earlier work by Ng et al. [1999] for deblurring images, but has not been exploited for lensing. The modification allows the product $\nabla^4 p$ in the objective function, Equation (4), to be expressed as a convolution via the Fourier convolution theorem since the system matrix resulting from discretizing Equation (4) is circulant. This enables the use of faster Fourier-domain solves in place of slower general-purpose iterative linear solvers.

We build on the method summarized in Section 3.2 and note that, for periodic boundary conditions, this problem can be solved very efficiently in Fourier space by using *proximal operators* [Parikh and Boyd 2013]. Proximal methods from sparse optimization allow for regularization to be imposed without destroying the structure of the system.

The specific proximal method that we use is a nonlinear variant (Algorithm 1) of the well-known *proximal point method*. The proximal point method is a simple fixed-point iteration defined by Equation (5), that is, expressed in terms of the *proximal operator*, $\text{prox}_{\gamma F}(p(\mathbf{x}))$, of the objective function $F(p(\mathbf{x}))$:

$$p^{k+1}(\mathbf{x}) \leftarrow \text{prox}_{\gamma F}(p^k(\mathbf{x})). \quad (5)$$

For an arbitrary convex function, $F(q(\mathbf{x}))$, the proximal operator, $\text{prox}_{\gamma F}$, (defined in Equation (6)) acts like a single step of a trust

region optimization in which a value of $p(\mathbf{x})$ is sought that reduces F but does not stray too far from the input argument $q(\mathbf{x})$:

$$\text{prox}_{\gamma F}(\mathbf{q}) = \arg \min_{\mathbf{p}} F(\mathbf{p}) + \frac{\gamma}{2} \|\mathbf{p} - \mathbf{q}\|_2^2. \quad (6)$$

To simplify notation, we use bold lowercase letters to refer to raster images, that is, $\mathbf{p} = p(\mathbf{x})$, noting that there is an implied discretization step. The parameter γ serves to trade off the competing objectives of minimizing F while remaining close (proximal) to \mathbf{q} , but for strictly convex objectives does not affect the final solution, only the number of iterations required to reach it.

For a least-squares objective $F(\mathbf{p}) = \frac{1}{2} \|\mathbf{A}\mathbf{p} - \mathbf{b}\|_2^2$, the resulting proximal operator [Parikh and Boyd 2013] is found by expanding the resulting right-hand side from Equation (6) and setting the gradient of the minimization term to zero. This results in Equation (7):

$$\text{prox}_{\gamma F}(\mathbf{q}) = (\gamma + \mathbf{A}^T \mathbf{A})^{-1} (\gamma \mathbf{q} + \mathbf{A}^T \mathbf{b}). \quad (7)$$

In our case, the function F is simply the integral term from Equation (4). We form the proximal operator by discretizing the integral with sums over image pixels and defining: $\mathbf{A} = f \nabla^2$ and $\mathbf{b} = 1 - i_p(\mathbf{x})$.

Since proximal operators contain a strictly convex regularization term, $\|\mathbf{p} - \mathbf{q}\|_2^2$, the whole operator is a strictly convex function even if F is only weakly convex, as is the case for our problem. The proximal regularization improves the conditioning of our problem and can be interpreted as *disappearing Tikhonov regularization* [Parikh and Boyd 2013], that is, regularization whose effect diminishes to zero as the algorithm converges. This is helpful since the added regularization does not distort the solution.

Another benefit is that proximal regularization does not change the structure of our problem since it only adds an identity term. This, coupled with the mirrored padding periodic boundary conditions, means that all terms in Equation (4) can be expressed as convolutions and the proximal operator solved in the Fourier domain. This is vastly more efficient than solving the optimization implied by the proximal operator in the spatial domain.

By denoting the forward and inverse Fourier transforms as $\mathcal{F}()$ and $\mathcal{F}^{-1}()$ respectively, complex conjugation by $*$ and performing multiplication and division pointwise, the proximal operator for Equation (7) can be re-expressed in the Fourier domain as Equation (8) for circulant matrices \mathbf{A} , as reported in Chambolle and Pock [2011], who used it to solve deconvolution problems:

$$\text{prox}_{\gamma F}(\mathbf{q}) = \mathcal{F}^{-1} \left(\frac{\mathcal{F}(\mathbf{b})\mathcal{F}(\mathbf{A})^* + \gamma \mathcal{F}(\mathbf{q})}{\mathcal{F}(\mathbf{A})^2 + \gamma} \right). \quad (8)$$

In practice, we modify Equation (8) slightly by the addition of a regularization parameter α that favors low-curvature solutions. The modified proximal operator is shown in Equation (9).

$$\text{prox}_{\gamma F}(\mathbf{q}) = \mathcal{F}^{-1} \left(\frac{\mathcal{F}(\mathbf{b})\mathcal{F}(\mathbf{A})^* + \gamma \mathcal{F}(\mathbf{q})}{(1 + \alpha)\mathcal{F}(\mathbf{A})^2 + \gamma} \right) \quad (9)$$

The constant $\alpha \geq 0$ regularizes the solution by favoring results with low curvature. This corresponds to solving a modified form of Equation (4) that imposes a penalty of $\frac{\alpha}{2} \|\nabla^2 p(\mathbf{x})\|^2$ once discretized (the second term of Equation (10) in the continuous case):

$$\begin{aligned} \hat{p}(\mathbf{x}) = \arg \min_{p(\mathbf{x})} & \int_{\mathbf{x}} (i_p(\mathbf{x}) - 1 + f \cdot \nabla^2 p(\mathbf{x}))^2 d\mathbf{x} \\ & + \alpha \int_{\mathbf{x}} (\nabla^2 p(\mathbf{x}))^2 d\mathbf{x}. \end{aligned} \quad (10)$$

ALGORITHM 1: Paraxial Caustics in Fourier Space

```
// Initialize phase surface as a constant value
 $p^0(\mathbf{x}) \leftarrow 0$ 
// Initialize iteration counter and constant parameters
 $\mathbf{A} \leftarrow f \nabla^2$ 
 $k \leftarrow 0$ 
while  $k < k_{\max}$  do
  // Warp target image by current solution
   $i_p^k(\mathbf{x}) \leftarrow i(\mathbf{x} + f \nabla p^k(\mathbf{x}))$ 
  // initialize right-hand side of least-squares problem
   $\mathbf{b} \leftarrow 1 - i_p^k(\mathbf{x})$ 
  // Update the current solution by evaluating
  // the proximal operator in Equation (9)
   $p^{k+1}(\mathbf{x}) \leftarrow \text{prox}_{\gamma F}(p^k(\mathbf{x}))$ 
  // update iteration index
   $k \leftarrow k + 1$ 
end while
// RETURN computed mapping
return  $p^{k_{\max}}(\mathbf{x})$ 
```

The effect of the parameter α is to favor smoother solutions than can otherwise be found. This helps to prevent the method from producing undesirable caustics in an attempt to achieve very bright highlights at the expense of image quality in darker regions. The effect of the α parameter is shown in Figure 5 for lens simulations.

Our final algorithm is shown in Algorithm 1 and is identical to the proximal point method except that the \mathbf{b} image used by the proximal operator is updated at every iteration using the warping procedure from our previous work [Damberg and Heidrich 2015]. After pre-computing the Fourier transforms of $f \nabla^2$, each iteration of the algorithm can be implemented with an image warping, some componentwise operations, and a forward/inverse Fourier transform.

4.1 Implementation

The reformulation of the algorithm results in orders of magnitude speedup when executed on a CPU using FFT-based solvers over the QMR solver that was previously used. Typical per-frame computation times were previously on the order of 20min or more [Damberg and Heidrich 2015], while the Fourier version in Algorithm 1 takes approximately 0.6s at the same resolution (256×128) on a Core i5 desktop computer, a speedup of approximately 2,000 times. The conversion to Fourier domain solves also results in operations that are more friendly for parallel GPU implementation. We have implemented the algorithm both in C++ and in CUDA, using CUFFT for the forward and inverse Fourier transforms [NVIDIA 2015]. The CUDA and CUFFT version of the code yields nearly a 150 times speedup over the single-threaded CPU version when run on a GeForce 770 GPU, resulting in roughly a 300,000-fold speedup over the naïve CPU version implemented using QMR. To our knowledge, this makes the algorithm the first freeform lensing method capable of operating in real time (see Table II). This is in contrast to methods such as Schwartzburg et al. [2014], which produce very-high-quality results, but have runtimes roughly five orders of magnitude higher than our GPU algorithm.

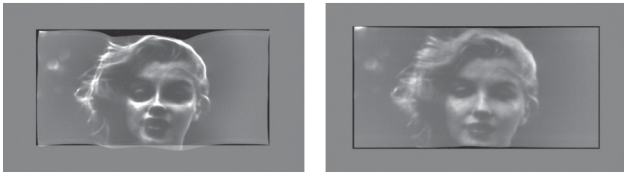
The algorithm is well suited to hardware implementation on devices such as GPUs, FPGAs, or ASICs due to its use of highly parallel FFTs and componentwise operations. We run Algorithm 1 for a fixed number of iterations (typically 10 or less). Convergence

Table II. Runtimes for Various Resolution Inputs with 10 Iterations of Algorithm 1

Algorithm	Resolution	Runtime (ms)	FPS
CPU	256 × 128	600ms	1.7
GPU	256 × 128	4ms	250
GPU	480 × 270	14ms	71
GPU	960 × 540	52ms	19
GPU	1920 × 1080	212ms	4.7



(a) Padded target



(b) Without padding

(c) Mirrored padded

Fig. 4. By mirror padding the input image, pure-Neumann boundary conditions at the image edge can be achieved while retaining a Toeplitz matrix structure. This prevents distortions of the image boundary. Results were simulated with LuxRender.

to a solution is rapid, requiring well fewer than 10 iterations. However, for many hardware implementations, it is desirable to have computation times that are independent of frame content.

4.2 Simulation Results

Using the equivalence between physical lenses and phase functions allows solid lens models to be generated for testing via geometric optics simulation (we use Blender+LuxRender). Examples are shown in Figure 4 and 5 which illustrate the effect of mirror padding and the choice of α respectively.

4.3 Static Phase Plates

We evaluate a selection of phase patterns using static phase plates with dimensions comparable to that of a phase-only SLM (approximately 12mm × 7mm). Figure 6 shows two phase plates that were manufactured on a fused silica wafer using a lithography-based process as well as the resulting light fields when illuminated with a collimated laser beam. The spatial resolution of the phase pattern is high at 12,288 × 6912 pixels per lens (1.00 μm pixel pitch). The phase resolution was limited to 8 phase levels (4 masks in the lithography process resulted in 8 phase levels between 0 and 2 π). The static phase plates were manufactured to evaluate our freeform lenses for static beam shaping applications and to test the method on high power, in this case, fiber-coupled lasers in which spatial coherence properties are partially destroyed. The laser used for

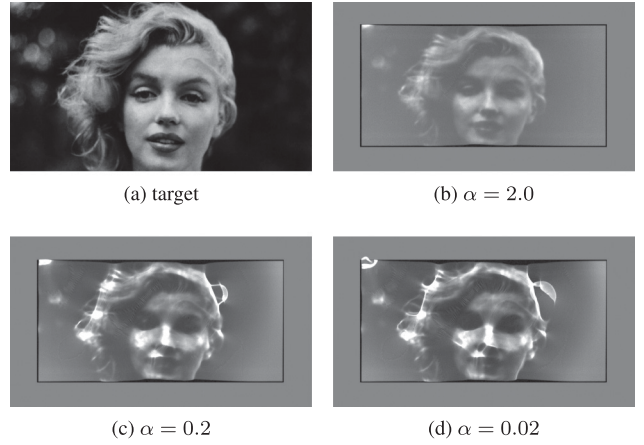


Fig. 5. LuxRender raytracing simulations: the smoothness parameter α penalizes strong caustics in the image that achieve high brightness but poor image quality.

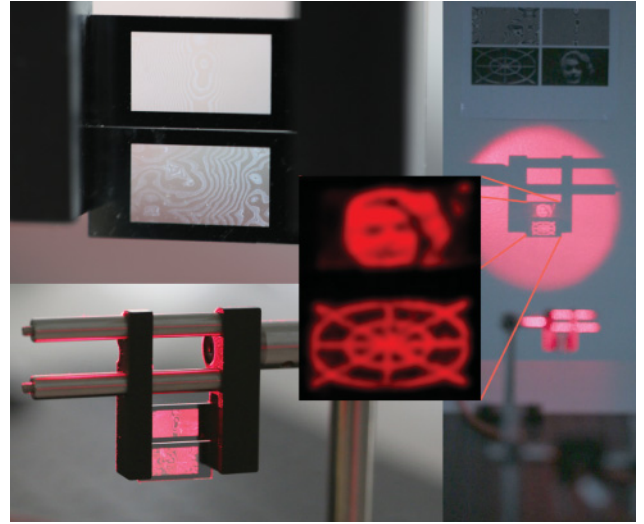


Fig. 6. Static phase plates manufactured on a fused silica wafer for two test patterns (Marilyn and Align). Left: Phase plates without and with laser illumination. The top phase plate reproduces *Marilyn*, the lower phase plate focuses the *Align* pattern. Right: The fiber-coupled and beam expanded laser light source, as well as two phase plates mounted in the light path (out of focus in the photo), are shown in the foreground. The projected structured illumination pattern is focused on the screen. For reference, above the red projection is a printed copy of the phase pattern etched into the wafer as well as a printout of a wave-front simulation of the expected intensity distribution on screen. The light pattern visually matches the simulation well.

experiments (see results in Figure 6) is a 638nm laser with up to 60W optical power. A suitable lens is used to expand the beam and to provide an approximately collimated (but slightly diverging) beam of light to illuminate the phase plates. Spatial coherence is partially destroyed as multiple laser sources within the module are combined and coupled into a 400 μm fiber, which integrates light traveling along multiple light paths. The ability to focus light from this source perfectly is limited (this applies not only to our phase plates, but also to ordinary glass lenses and other optics);

thus, the sharpness of the resulting image is affected. For the proposed use case as a structured light source in a projection system, a small amount of blur in the image is acceptable, if not desirable. The ray-tracing simulations in Section 4.2 begin with a model of a near-perfectly collimated light source (a distant point light source), and are therefore sharper than the image produced by our experimental phase plate (due to divergence of the beam). However, the overall geometry of the experimental light distribution appears visually undistorted and the image contrast is comparable to that of the simulations. For the projector prototype described in Section 5, we use a free space laser and achieve a similar amount of blur with a diffuser.

5. DYNAMIC LENSING IN PROJECTION SYSTEMS

In order to apply the freeform lens concept in projection displays, we require a spatial light modulator that can manipulate the shape of the wavefront of reflected or transmitted light. We first provide a brief overview of the different technologies available for this purpose, then describe experiments and prototypes using the technology.

There are several commercially available technologies that can rapidly manipulate the phase of an incident wavefront in order to modulate phase. These include microelectromechanical (MEMS) displays such as analog mirror arrays [Hoskinson et al. 2012] or deformable mirrors used in wavefront sensing and correction. The benefit of MEMS-based devices is the very fast temporal response. Disadvantages include cost and availability as well as the relatively low spatial resolution: devices with 4096 actuators are considered high resolution in this domain, leaving a resolution gap of 3 orders of magnitude to common projection displays.

An alternative to MEMS-based mirrors is offered by liquid crystal displays either in the form of a transmissive LCD or in a reflective configuration: liquid crystal on silicon (LCoS). Liquid crystal displays can retard the phase of light and offer high spatial resolution. Reflective LCoS devices can update at higher switching speeds compared to transmissive LCD due to the reduced cell gap, and also provide a high pixel fill factor. Omitting the input/output polarizing beam splitter and carefully managing the polarization state of incoming light allows for the operation in phase-only mode, in which the phase is retarded based on the rotation amount of the liquid crystals at each pixel location. Although standard LCoS modules can be used as phase modulators in principle, dedicated displays are available that can be calibrated to shift the phase by one wavelength or more, which allows for the implementation of “steeper” lenses that steer light more aggressively. The pixel values of the LCoS module then correspond directly to the wavelength-modulated phase function, that is, $\text{mod}(p(x), \lambda)$. For more on this topic, we refer the reader to Robinson et al. [2005].

Our choice of phase SLM is a reflective LCoS chip distributed by Holoeye Photonics AG [2015]. It provides a spatial resolution of 1920×1080 pixels at a pixel pitch of $6.4 \mu\text{m}$, and can refresh at up to 60Hz. Access to a lookup table allows for calibration of the modulator for different working wavelengths. The fill factor and reflectivity of the display are high compared to other technologies at 93% and 75%, respectively. The phase retardation is calibrated to between 0 and 2π , equivalent to one wavelength of light.

This is sufficient to generate freeform lenses with a long focal distance. For shorter focal distances, we require more strongly curved wavefronts, which creates larger than 2π values for $p(\cdot)$. We can address this issue by *phase wrapping*, that is, using the fractional part of $p(\cdot)$ to control the SLM that results in patterns similar to a Fresnel lens. A simple example to demonstrate this technique is

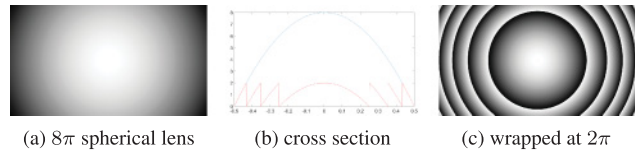


Fig. 7. *Phase wrapping* example: (a) phase function of a spherical lens with a height of 8π , (b) a plot of the cross-section of the original and the phase wrapped lens, and (c) the same lens wrapped at intervals of 2π .

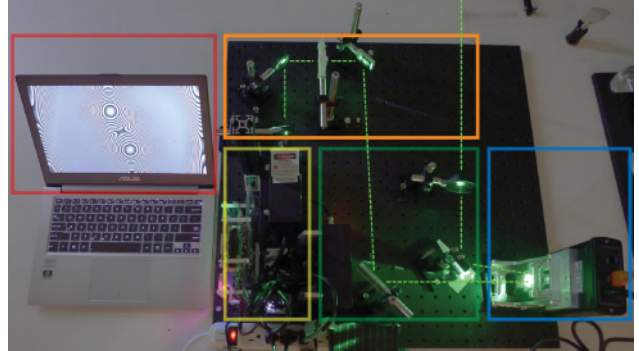


Fig. 8. Phase modulation test setup consisting of a light source (yellow box, 532nm DPSS laser and laser controller), beam expansion and collimation optics and folding mirrors (orange box), the reflective phase SLM (blue box), various folding mirrors, and a simple projection lens to relay the image from an intermediate-image plane onto the projection screen (green box). The image is formed in an intermediary image plane between the phase modulator and the projection lens. We empirically determine the type and position of a diffuser (not depicted) close to this intermediate-image plane to produce the light profile in Figure 11. The gray scale intensity of the phase pattern shown on the computer screen correlates linearly to the desired phase retardation in the optical path to form the image. This pattern has been phase-wrapped at multiples of one wavelength and can be addressed directly onto the microdisplay.

presented in Figure 7 (also, see the red box in Figure 8 as well as the phase patterns in Figures 11 and 12).

5.1 Prototype

We initially analyze results from the first (phase) modulation stage in isolation (see Figure 8) and later relay the resulting light profile into the second stage for amplitude attenuation. The intermediate results that can be seen in Figure 11 are a product of tuning the type and position of the diffuser in the setup in Figure 8. Later, the simple projection lens in Figure 8 was replaced with a relay lens with an appropriate focal distance to couple the diffused light profile into the projection head (see Figures 9 and 10).

The use of single-mode lasers causes small-scale artifacts including screen speckle and diffraction *fringes* due to interference (Figure 11, center photo). Artifacts of this nature can be reduced below the visible threshold by using, for example, a different type of laser light source (e.g., as in Section 4.2), or a set of lasers with different center wavelengths, or broadband light sources such as LEDs and lamps, as used in our previous work [Damberg and Heidrich 2015]. When constrained to using a narrow-band laser light source such as in our test setup, a similar image *smoothing* effect can be achieved by spatially or temporally averaging the image using, for example, a diffuser or commercially available continuous deformable mirrors

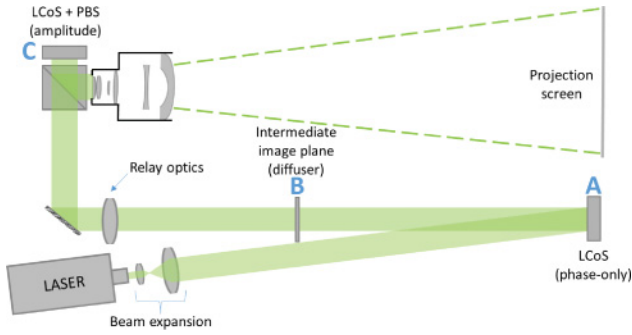


Fig. 9. System diagram of the proposed and prototyped high-brightness HDR projector: light from an expanded and collimated laser beam is reflected off a phase-only modulator (A). The per-pixel amount of phase retardation resembles the height field of the dynamic lens calculated with our algorithm. The effective focal plane of this freeform lens is in-plane with a diffuser (B), which in turn is relayed onto the image plane of an off-the-shelf, reflective projection head (C) consisting of the polarizing beam splitter together with an LCoS microdisplay and a projection lens. Light from dark parts of the image can be used to create high-luminance features, and simultaneously reduce the black level.

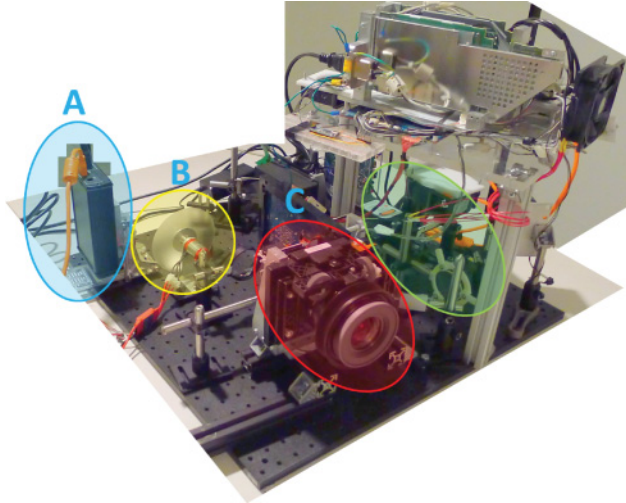


Fig. 10. Prototype system used for results photographs in Figures 11 and 12 including laser light source and both the light steering as well as the amplitude modulation stage. Positions A (blue, phase modulator), B (yellow, diffuser) and C (red, amplitude modulation and projection optics) correlate to the positions labeled in Figure 9. The green marked area holds the laser light source, the remainder of the photos is mounting hardware and control electronics.

that introduce slight angular diversity in a pseudo-random fashion at high speeds. For ease of implementation, we choose a structured (holographic) diffuser with half angle of 0.5° , which is placed in an intermediate image plane following the phase SLM. Such diffusers are available at high transmission efficiencies of $>90\%$. A photo of the *cleaned-up* intensity profiles can be seen in Figure 11, right.

At a high level, the light path of a traditional projection system consist of a high-intensity light source and some form of beam shaping: for example, beam expansion, collimation and homogenization, color separation, and recombining optics. At the heart of a typical projector, a small SLM attenuates the amplitude of light

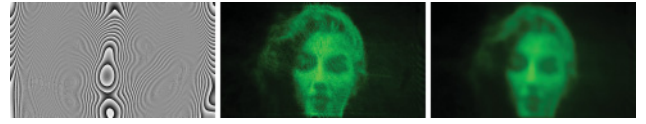


Fig. 11. From left to right, correlating to positions A to C in Figure 9: (A) phase pattern present at phase-only LCoS modulator; (B) direct image produced by lens in intermediary image plane (prior to diffuser); and (C) intensity distribution present at amplitude LCoS modulator after having passed through a thin diffuser.

per pixel. The resulting image is then magnified and imaged onto the projection screen. We integrate the laser light source as well as the phase-only modulation stage and diffuser into the architecture of an existing projector and demonstrate a high-brightness, high-dynamic range projection system, in which a structured light field is formed based on the new dynamic lensing method. Additional sharpness and contrast is provided using a traditional LCoS-based amplitude-modulating microdisplay.

We make use of the forward-image formation model from our simulations to predict the illumination profile present at the second, amplitude-only modulator. Given the phase function from the freeform lensing algorithm, the light distribution on the image plane is predicted using the simple model from Equations (1) and (2). The amount of smoothness introduced at the diffuser at the intermediate-image plane can be modeled using a blur kernel (system point spread function that can be either directly measured or computed via deconvolution for known targets); the modulation pattern required for the amplitude modulator is then obtained to introduce any missing spatial information as well as additional contrast where needed. We note that careful calibration and characterization of the entire optical system is required to optimally control the SLMs. No significant efforts beyond careful spatial registration of the two images (illumination profile caused by phase retardation and amplitude modulation on the SLM) and calibration to linear increments in light intensity were performed for this work.

5.2 Results

Figure 11 shows the phase patterns computed by Algorithm 1 as applied to the phase modulator, with black corresponding to no phase retardation and white corresponding to a retardation of 2π . We illustrate how phase patterns with maximum phase retardation larger than 2π can be wrapped to the maximum phase retardation of the modulator, resulting in a pattern similar to a Fresnel lens. The resulting light profile resembles the target image closely, but also contains a small amount of local, high-spatial frequency noise. We make use of a high transmission efficiency patterned diffuser (0.5° half-angle) to integrate over these local intensity variations. The resulting light profile at the diffuser is locally smooth and still provides sufficient contrast to enhance peak luminance and lower black level significantly.

Figure 12 shows a selection of experimental results for our method. The first row of Figure 12 shows the phase pattern addressed onto the phase SLM. In the second row of Figure 12, we show photos of the light-steering, high-brightness projector and compare them to what a traditional projector with the same lumen rating out of lens would look like (third row). For the latter case, we simply address a flat phase across the phase SLM. The last two rows show false-color logarithmic luminance plots on the same scale for the traditional (bottom) and light-steering projector (fourth row) systems. All photos were captured with identical camera settings and show that our method not only recovers better black levels but

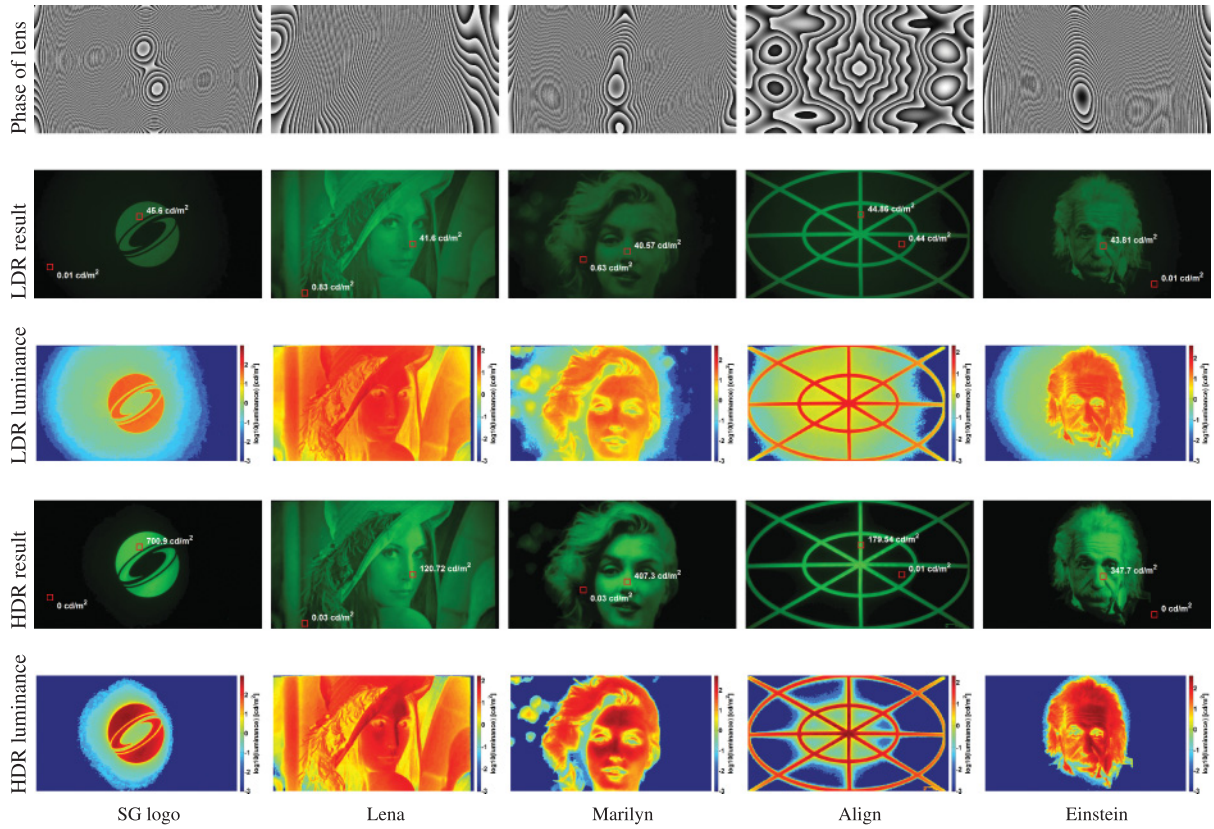


Fig. 12. Result photos and measurements of the HDR prototype projector. Top to bottom: *Phase function of lens*. The phase pattern as computed by Algorithm 1. *LDR projector for comparison*. The same projector power (out of lens) used in a traditional, light-attenuating mode: a uniform light field (flat phase field) is provided to the amplitude SLM, which forms the image by blocking light. *LDR luminance profile on a logarithmic scale*. *HDR projector*. Photograph of our lensing approach used to redistribute light from dark regions to bright regions, resulting in improved black levels and significantly increased highlight intensity. *HDR luminance profile on a logarithmic scale*.

Table III. Luminance Measurements of the Results Depicted in Figure 12

Name	Power (relative)	HDR L_{peak} [cd/m^2]	HDR L_{black} [cd/m^2]	HDR contrast	LDR L_{peak} [cd/m^2]	LDR L_{black} [cd/m^2]	LDR contrast	L_{peak} gain	Contrast gain
SG logo	7%	701	0.001	700900 : 1	46	0.01	4,272 : 1	15X	173X
Lena	48%	121	0.03	4053 : 1	42	0.83	50 : 1	3X	80X
Marilyn	23%	407	0.03	13008 : 1	41	0.63	64 : 1	10X	203X
Align	20%	180	0.01	29677 : 1	45	0.44	101 : 1	4X	292X
Einstein	15%	348	0.001	347700 : 1	44	0.01	2,996 : 1	8X	122X

Note: Multiple exposures at varying exposure times were captured (8s, 4s, 2s, 1s, 1/2s, 1/4s, 1/8s, 1/15s, 1/30s, 1/60s, 1/125s) and combined into one linear HDR file, which was then calibrated to represent actual luminance values using a luminance spot meter (Minolta LS100). The lowest accurate measurement using the Minolta LS100 is 0.001 cd/m^2 .

also allows for increased luminance of highlights by redistributing light from dark regions of the image to lighter regions, making better use of available power and enabling high-brightness, high-dynamic range projection with drastically reduced power consumption. Table III contains measured black level and peak luminance data for both the LDR and HDR cases for each of the test images. The L_{peak} gain and contrast gain entries in the right columns summarize the merit of the proposed approach. While HDR images are unlikely to have as high of an APL as, for example, the second test image (48%), a gain in peak luminance of 3X, while costly, might be feasible to produce with existing projection technologies (e.g., by using a high-gain screen or a very-high-power light source). The black level of such a system would also be elevated by a factor of

3X. Achieving a gain in L_{peak} of 10X to 15X (such as in some of the other test cases) using traditional projector technologies is not feasible, both because of light source power limitations and due to visibly elevated black levels. We note that the contrast numbers presented in the table represent the *in-scene* contrast rather than a sequential contrast.

5.3 Limitations and Future Work

The prototype architecture presented in this work and the resulting image-quality improvements in contrast and peak luminance that can be achieved with it demonstrate the feasibility of the concept. We briefly want to discuss some of the obvious and less obvious

limitations of the implementation. We believe that, while nontrivial, most of these limitations can be addressed with a modest amount of further engineering work.

- The test system was built with a single, monochromatic (green) light source. For a full-color projector, at least two additional color channels will need to be added to the system in either a parallel or a time-sequential fashion. Either approach presents its own (solved) challenges: the former with respect to alignment of red, green, and blue components, such as SLM and dichroic mirrors, and the latter with respect to synchronization/timing and thermal limitations.
- As with any display based on narrow-band or monochromatic light sources (such as LEDs or lasers), care needs to be taken to manage undesirable properties such as observer metamerism and speckle.
- The phase SLM and the amplitude SLM need to be synchronized, ideally at the frame or subframe level. The amplitude modulator in the prototype was borrowed from a consumer projector, which introduced an undesired latency in one of the modulation stages.
- In a full-color system, sufficient colorimetric calibration will be possible only by characterizing and accurately modeling the system, including the PSF, which, depending on the light source and optical path, could potentially be dependent on location or even feature size.
- None of the relay optics or other elements was custom designed for the prototype, which leads to light losses. Even with a more optimized light path, the addition of a phase SLM can reduce the overall light throughput. We estimate that this loss can be as high as 40% to 60% for the components used in the prototype. While this might seem high, we note that even for bright images (APL of 50%) the gain in peak luminance exceeds what could be achieved in a traditional projector. Better suitable SLMs can further reduce the associated light losses.
- Careful alignment of a number of elements in the light path is required to achieve a uniform and predictable light profile on the phase modulator. In our experiment, the reflective nature of the phase SLM required off-axis illumination that was not accounted for in the simulations and algorithm, which, in turn, leads to errors in the resulting luminance profiles. While these errors were not clearly visible in the images projected onto the screen, the logarithmic luminance representation in Figure 12 reveals this nonuniformity. It can be accounted for in the lens pattern.
- Finally, the dynamic nature of the projection system with respect to peak luminance and feature size may present a challenge when color grading content for the display. The notion of a limited light budget and a peak luminance that exceeds that of full-screen white might make sense from an HDR image statistics point of view, but would require a rethinking in existing movie production processes.

6. DISCUSSION AND CONCLUSIONS

We have made two technical contributions: a simple, but fast and effective, new optimization method for freeform lenses (goal-based caustics), and a new dual-modulation design for projection displays, which uses a phase-only spatial light modulator as a programmable freeform lens for HDR projection.

The new freeform lens optimization approach is based on first-order (paraxial) approximations, which hold for long focal lengths and are widely used in optics. Under this linear model, the local deflection of light is proportional to the gradient of a phase

modulation function, while the intensity is proportional to the Laplacian. We combine this insight with a new parameterization of the optimization problem in the *lens plane* instead of the image plane to arrive at a simple-to-implement method that optimizes directly for the phase function without any additional integration steps. Solved in the Fourier domain, this is the first algorithmic approach for freeform lensing that is efficient enough for on-the-fly computation of video sequences.

Our new dual-modulation HDR projector design finally allows perceptually meaningful gains in peak luminance on large cinema screens while simultaneously improving black level performance and maintaining a manageable power, light, and cost budget. As such, we believe that the approach presents one of the most sensible proposals to date for commercial high-contrast HDR projection systems and one of the most practical ways to achieve high-brightness HDR imagery in cinema.

ACKNOWLEDGMENTS

The authors would like to thank Qiang Fu for spending many hours manufacturing the two static phase plates in the nanofab lab at KAUST and gratefully acknowledge Anders Ballestad's contributions to Section 3.1, especially the hand-tuning of all 104 HDR images to determine the appropriate scaling factors for dark viewing environments.

REFERENCES

- M. V. Berry. 2006. Oriental magic mirrors and the Laplacian image. *European Journal of Physics* 27, 1, 109.
- Oliver Bimber and Daisuke Iwai. 2008. Superimposing dynamic range. *ACM Transactions on Graphics* 27, 5, 150.
- G. H. Blackham and A. R. Neale. 1998. Image display apparatus. Retrieved January 30, 2016 from <http://www.google.ca/patents/EP0829747A1?cl=en> EP Patent App. EP19,970,306,624.
- Edward Buckley. 2008. 70.2: Holographic laser projection technology. In *Proceedings of SID*, Vol. 39. 1074–1079.
- Antonin Chambolle and Thomas Pock. 2011. A first-order primal-dual algorithm for convex problems with applications to imaging. *Journal of Mathematical Imaging and Vision* 40, 1, 120–145.
- Gerwin Damberg and Wolfgang Heidrich. 2015. Efficient freeform lens optimization for computational caustic displays. *Optics Express* 23, 8, 10224–10232.
- Gerwin Damberg, Helge Seetzen, Greg Ward, Wolfgang Heidrich, and Lorne Whitehead. 2007a. 3.2: High dynamic range projection systems. In *Proceedings of SID*, Vol. 38. Wiley Online Library, 4–7.
- Gerwin Damberg, Helge Seetzen, Greg Ward, Michael Kang, Peter Longhurst, Wolfgang Heidrich, and Lorne Whitehead. 2007b. High dynamic range projector. In *SIGGRAPH Emerging Technologies*.
- Mark D. Fairchild. 2007. The HDR photographic survey. In *Color and Imaging Conference*, Vol. 2007. Society for Imaging Science and Technology, 233–238.
- Manuel Finckh, Holger Dammertz, and Hendrik P. A. Lensch. 2010. Geometry construction from caustic images. In *Proceedings of ECCV*. 464–477.
- Paul R. Haugen, Hartmut Bartelt, and Steven K. Case. 1983. Image formation by multifacet holograms. *Applied Optics* 22, 18, 2822–2829.
- Holoeye Photonics AG. 2015. Spatial light modulators. Retrieved January 30, 2016 from <http://www.holoeye.com> (2015).

- Reynald Hoskinson, Stefan Hampl, and Boris Stoeber. 2012. Arrays of large-area, tip/tilt micromirrors for use in a high-contrast projector. *Sensors and Actuators A: Physical* 173, 1, 172–179.
- Reynald Hoskinson, Boris Stoeber, Wolfgang Heidrich, and Sidney Fels. 2010. Light reallocation for high contrast projection using an analog micromirror array. *ACM Transactions on Graphics* 29, 6, 165.
- Matthias B. Hullin, Ivo Ihrke, Wolfgang Heidrich, Tim Weyrich, Gerwin Damberg, and Martin Fuchs. 2013. State of the art in computational fabrication and display of material appearance. In *Eurographics Annual Conference (STAR)*.
- Thomas Kiser, Michael Eigensatz, Minh Man Nguyen, Philippe Bompas, and Mark Pauly. 2013. Architectural caustics: Controlling light with geometry. In *Advances in Architectural Geometry 2012*. Springer, 91–106.
- Y. Kusakabe, M. Kanazawa, Y. Nojiri, M. Furuya, and M. Yoshimura. 2009. A high-dynamic-range and high-resolution projector with dual modulation. *Proceedings of SPIE* 7241, 72410Q–72410Q–11.
- L. B. Lesem, P. M. Hirsch, and J. A. Jordan. 1969. The kinoform: A new wavefront reconstruction device. *IBM Journal of Research and Development* 13, 2, 150–155.
- Juan C. Miñano, Pablo Benítez, and Asunción Santamaría. 2009. Free-form optics for illumination. *Optical Review* 16, 2, 99–102.
- Michael K. Ng, Raymond H. Chan, and Wun-Cheung Tang. 1999. A fast algorithm for deblurring models with Neumann boundary conditions. *SIAM Journal on Scientific Computing* 21, 3, 851–866.
- NVIDIA. 2015. Programming Guide, CUSPARSE, CUBLAS, and CUFFT Library User Guides. <https://docs.nvidia.com/cuda/cuda-c-programming-guide/index.html>.
- Marios Papas, Thomas Houit, Derek Nowrouzezahrai, Markus Gross, and Wojciech Jarosz. 2012. The magic lens: Refractive steganography. *ACM Transactions on Graphics* 31, 6, 186.
- Marios Papas, Wojciech Jarosz, Wenzel Jakob, Szymon Rusinkiewicz, Wojciech Matusik, and Tim Weyrich. 2011. Goal-based caustics. *Computer Graphics Forum* 30, 2, 503–511.
- Neal Parikh and Stephen Boyd. 2013. Proximal algorithms. *Foundations and Trends in Optimization* 1, 3, 123–231.
- Mark Pauly and Thomas Kiser. 2012. *Caustic Art*. Technical Report. EFPL (École polytechnique fédérale de Lausanne), Switzerland. http://lgg.epfl.ch/publications/2012/caustics/caustic_art.pdf.
- Erik Reinhard, Tania Pouli, Timo Kunkel, Ben Long, Anders Ballestad, and Gerwin Damberg. 2012. Calibrated image appearance reproduction. *ACM Transactions on Graphics* 31, 6, 201.
- A. Rempel, W. Heidrich, H. Li, and R. Mantiuk. 2009. Video viewing preferences for HDR displays under varying ambient illumination. *Proceedings of APGV*. 45–52.
- A. Rempel, W. Heidrich, and R. Mantiuk. 2011. The role of contrast in the perceived depth of monocular imagery. *Proceedings of APGV*. 115.
- Michael D. Robinson, Gary Sharp, and Jianmin Chen. 2005. *Polarization Engineering for LCD Projection*. Vol. 4. John Wiley & Sons, Hoboken, NJ.
- Y. Schwartzburg, R. Testuz, A. Tagliasacchi, and M. Pauly. 2014. High-contrast computational caustic design. *ACM Transactions on Graphics (TOG)* 33, 4, 74.
- Helge Seetzen. 2009. *High Dynamic Range Display and Projection Systems*. Ph.D. Dissertation. University of British Columbia, Vancouver, BC.
- H. Seetzen, W. Heidrich, W. Stuerzlinger, G. Ward, L. Whitehead, M. Trentacoste, Ghosh, and A. Vorozcovs. 2004. High dynamic range display systems. *ACM Transactions on Graphics (Proceedings SIGGRAPH)*, 760–768.
- David J. Silvester and Milan D. Mihajlović. 2004. A black-box multigrid preconditioner for the biharmonic equation. *BIT Numerical Mathematics* 44, 1, 151–163.
- X. H. Tang and C. I. Christov. 2006. An operator splitting scheme for biharmonic equation with accelerated convergence. In *Proceedings of the 5th International Conference on Large-Scale Scientific Computing (LSSC'05)*. Springer, Berlin, 387–394. DOI: http://dx.doi.org/10.1007/11666806_44
- Yonghao Yue, Kei Iwasaki, Bing-Yu Chen, Yoshinori Dobashi, and Tomoyuki Nishita. 2012. Pixel art with refracted light by rearrangeable sticks. *Computer Graphics Forum* 31, 2pt3 (2012), 575–582.
- Y. Yue, K. Iwasaki, B.-Y. Chen, Y. Dobashi, and T. Nishita. 2014. Poisson-based continuous surface generation for goal-based caustics. *ACM Transactions on Graphics (TOG)* 33, 3, 31.
- Jie Zhao. 2004. Convergence of V-cycle and F-cycle multigrid methods for the biharmonic problem using the Morley element. *Electronic Transactions on Numerical Analysis* 17, 112–132.
- M. Zink and M. D. Smith. 2015. Managing HDR content production and display device capabilities. *International Broadcasting Convention 2015*.

Received July 2015; revised November 2015; accepted December 2015